Surface & Coatings Technology 405 (2021) 126676

Contents lists available at ScienceDirect

Surface & Coatings Technology

journal homepage: www.elsevier.com/locate/surfcoat

Synthesis of carbon nanotube reinforced Al matrix composite coatings via cold spray deposition

Xinliang Xie [a,b,d,*], Zhanqiu Tan [c], Chaoyue Chen [e], Yingchun Xie [f], Hongjian Wu [a], Xingchen Yan [a,f], Shuohong Gao [a], Zhiqiang Li [c], Gang Ji [b,**], Hanlin Liao [a]

[a] ICB UMR 6303, CNRS, Univ. Bourgogne Franche-Comté, UTBM, F-90010 Belfort, France
[b] Univ. Lille, CNRS, INRA, ENSCL, UMR 8207 - UMET - Unité Matériaux et Transformations, F-59000 Lille, France
[c] State Key Laboratory of Metal Matrix Composites, Shanghai Jiao Tong University, Shanghai 200240, China
[d] Institute of Mechanics, Materials and Civil Engineering, UC Louvain, Louvain-la-Neuve, Belgium
[e] State Key Laboratory of Advanced Special Steels, School of Materials Science and Engineering, Shanghai University, Shanghai 200444, China
[f] National Engineering Laboratory for Modern Materials Surface Engineering Technology, Institute of New Materials, Guangdong Academy of Sciences, Guangzhou 510651, China

ARTICLE INFO

Keywords:
Al matrix composite
Carbon nanotube reinforced
Cold spray
Plastic deformation
Mechanical property

ABSTRACT

For the fabrication of high-strength carbon nanotube (CNT) reinforced Al matrix composites, the uniform dispersion, strong interface bonding and high structural integrity of CNTs have been regarded as the three most important issues. In this work, two distinct approaches, namely high shear dispersion (HSD) and shift-speed ball milling (SSBM), were applied to disperse CNTs (1.5 wt%) into pure Al powders. These two kinds of CNT/Al composite powders as well as the pure Al powder (as a comparison) were deposited onto stainless steel plates by cold spraying using different processing parameters. The velocity and the temperature of the particle prior to impact was simulated by the commercial code of Fluent. The deposition efficiency, microstructure evolution, as well as the distribution and structural integrity of CNTs in the composite coatings produced from different starting powders were comparatively investigated in terms of X-ray diffraction (XRD), Raman spectra, and electron back scanning diffraction (EBSD). According to the XRD and Raman analysis, no new phases such as oxides or brittle Al_4C_3 were detectable in both CNT/Al composite coatings. Some structural damages of CNTs were found in both composite coatings, especially the one fabricated from HSD composite powder. The dispersion of CNTs onto Al particle surfaces by HSD approach did not achieve a significant strengthening effect on the composite coatings, but adversely affected the metallic bonding of the particles and the substrate. The microhardness of the CNT/Al composite coating produced from SSBM powders reached around ~115 $HV_{0.1}$, showing a significant improvement compared to the pure Al coating mainly due to the grain refinement and CNTs strengthening.

1. Introduction

Owing to the ultrahigh strength, superior elastic modulus and large aspect ratio, carbon nanotubes (CNTs) have emerged as ideal nano-reinforcements for metal matrix composites [1,2]. It is expected that the use of CNTs as reinforcements can increase the strength and stiffness of a metal matrix. In the past decade, much attention has been increasingly paid to CNTs-reinforced aluminum matrix composites (hereafter called CNT/Al) because of their strong and light-weight properties. It has become a promising material candidate in aerospace and automobile industries [3,4].

For the fabrication of high-strength CNT/Al composites, the uniform CNTs dispersion, strong interface bonding and high structural integrity of CNTs have been regarded as the three most important issues [5]. To solve the CNT agglomeration problem, the techniques of nano-scale dispersion [6,7], high energy ball milling [8,9], in-situ grown method [10], flake powder metallurgy (PM) [11,12] and solution coating [13] have been developed in the past decade. Many research efforts have resorted to high energy ball milling to homogenously disperse CNTs in the Al matrix powder particles [9,14]. However, the structural integrity

* Correspondence to: X. Xie, ICB UMR 6303, CNRS, Univ. Bourgogne Franche-Comté, UTBM, F-90010 Belfort, France.
** Correspondence to: G. Ji, Univ. Lille, CNRS, INRA, ENSCL, UMR 8207 - UMET - Unité Matériaux et Transformations, F-59000 Lille, France
E-mail addresses: xinliang.xie@uclouvain.be (X. Xie), gang.ji@univ-lille.fr (G. Ji).

https://doi.org/10.1016/j.surfcoat.2020.126676
Received 1 October 2020; Received in revised form 19 November 2020; Accepted 22 November 2020
Available online 24 November 2020

of CNTs was often damaged by the impacting of milling balls, which proved to be detrimental for mechanical properties [9]. Very recently, a new flake powder metallurgy route via shift-speed ball milling strategy has been proposed by Xu.et al. [15]. The coordination of CNTs dispersion, integrity and interfacial bonding could be achieved in the CNT/Al composite powder [15].

Various consolidation processes including casting [16], thermal spraying [17], sintering [10] and hot-extrusion [9] were selectively applied during the fabrication process of CNT/Al composites. However, these methods all have their own limits. For example, the sintering process can efficiently produce dense composite structures. However, grain growth and aluminum carbide (Al_4C_3) formation due to interfacial reactions between the Al matrix and CNTs are inevitable during such a process, which might result in weakening of the composite [15]. During the thermal spray process (e.g. atmosphere plasma spray), CNTs are exposed to a high temperature and oxygen-rich environment, and therefore destruction and gasification can take place [17].

Recently, a newly emerged technique named cold spraying (CS), has been widely investigated in academic laboratories and applied in factory manufacturing [18,19]. In this process, micron-sized particles are accelerated to supersonic velocity (300–1200 m/s) via the expansion of a pressurized gas through a diverging-converging nozzle. Upon impact, powder particles undergo severe plastic deformation and bond to the substrate surface, allowing a rapid layer-by-layer deposition of metals or metal matrix composites [20,21]. The feedstock remains in the solid state throughout the entire process. Owing to its 'cold' feature, the deleterious effects of oxidation, phase transformation, decomposition, grain growth, and other problems can be minimized or eliminated [22,23]. Such significant advantages make CS a promising technique for several new applications, including the synthesis of CNTs-reinforced metal matrix composites and other temperature-sensitive materials [24,25]. So far, only a few works have been reported concerning the CNT/Al composite using CS process [26–28]. In the work of Srinivasa et al. [26], spray drying was used to disperse CNTs on the surface of micron-sized gas atomized Al—Si eutectic powders. However, fractured CNTs were found in the composite coating due to impact and shearing between Al—Si eutectic particles and Al matrix [26]. Nanoindentation of the composite yielded a variable elastic modulus values in the range from 40 to 120 GPa, which was attributed to microstructural heterogeneity of the coatings [26]. Kicheol et al. also used CS to produce nanocrystalline Al matrix composites reinforced with CNTs by using ball-milled composite powder [27,28]. The composites exhibited an intimate interface bonding state between the CNTs and nanocrystalline Al matrix. However, partial disconnections and fracture of the CNTs cannot be avoided during high-velocity impact [28]. These results demonstrate that the powder preparation approach can affect the distribution and structural integrity of CNTs in the composite, coating microstructure and finally mechanical properties. In addition, the initial states of the composite powder, including the particle morphology, CNTs distribution, and the strain stress, take critical role for composite deposition.

In this work, two distinct approaches, namely high shear dispersion (HSD) process and shift-speed ball milling (SSBM) process, were applied to disperse CNTs into pure Al powder particles. These two kinds of CNT/Al composite powders as well as pure Al powders (for comparison) were deposited onto stainless steel plates using a variety of processing parameters. The deposition efficiency (DE), microstructure, as well as structural integrity of CNTs in the coatings obtained by the different starting powders were comparatively investigated. Microhardness of the composite coatings was measured, and strengthening mechanisms related to microstructural evolution were discussed to reveal the role of CNTs.

2. Experimental details

2.1. Fabrication of the CNT/Al composite powder

As illustrated in Fig. 1, HSD and SSBM processes were applied for obtaining the composite powders with spherical and cake-like morphologies, respectively.

(1) HSD processing of the CNT/Al composite powder. During this process, the near-spherical pure Al powder having an average particle size of around 30 μm and 1.5 wt% multi-walled CNTs with the diameters of 15–30 nm and the lengths of 1–5 μm were firstly blended in a mixer for 30 min at a speed of 300 rpm. The mixture was then processed in a high-speed mechanical powder processor (Nobilta, Hosokawa Micron Corporation, Japan) at a speed of 1800 rpm for 15 min. As illustrated in Fig. 1a, the powder mixture was processed in a special designed container, in which a rotating four-way blade was almost touching the inner wall of the container with only a 3 mm gap. The application of controlled shear stress between the powder mixture allows the uniform distribution of CNTs on the surface of the Al particles.
(2) SSBM processing of the CNT/Al composite powder. Alternatively, the 1.5 wt% CNT/Al powders were prepared using flake powder metallurgy combined with shift-speed ball milling [15]. As shown in Fig. 1b, CNTs and pure Al powders were used as the starting materials, and stearic acid (3 wt%) was used as the process control agent. They were firstly mixed using a blender, and then the mixed powders were ball milled in a planetary ball mill at a speed of 200 rpm for 4 h with a ball-to-powder ratio of 10:1. Afterwards, the mixed powders were heat treated at 400 °C for 7 h to remove the stearic acid, and then milled at 270 rpm for 1 h to obtain cake-like CNT/Al powders.

2.2. Cold spray of the CNT/Al composite powder

Following the preparation of composite powders, these two kinds of CNT/Al composite powders as well as pure Al powders were deposited onto the stainless-steel plates (60 mm × 60 mm × 3 mm) by using a homemade CS system (LERMPS, UTBM, France). The nozzle with an expansion ratio of 8.3 was cooled by running water in order to prevent nozzle clogging and improve the reliability of this system. High-pressure compressed air and argon were used as powder carrier gas and propelling gas, respectively. The propellant gas at the nozzle inlet had a pressure of 3.0 MPa and a wide range of temperatures (300, 400, 500, and 550 °C). The standoff distance between the substrate and the nozzle exit was set to 30 mm. The nozzle traverse speed for coating deposition was set to 100 mm/s. Nozzle trajectory was repeated for 20 times to obtain a thick coating. The substrate surface was grit blasted prior to CS deposition.

The DE was determined by measuring the weights of the substrate (W_1), feedstock powder (W_2), substrate with coating (W_3), and the left-over feedstock powder (W_4) according to Eq. (1):

$$\mathrm{DE} = \frac{W_3 - W_1}{W_2 - W_4} \times 100\% \quad (1)$$

2.3. Numerical simulation

A computational fluid dynamics (CFD) model by the commercial code of Fluent (CFD; ANSYS Fluent Version 17.1) was developed to predict the velocity and the temperature of a particle prior to impact [29]. In order to save computational time, two-dimensional axisymmetric model was used for these three CS systems. More detailed description of this model can be found in our previous work [29,30]. The computational domain was meshed using a regular and structured grid of quadrilateral elements. In this model, particles were presented at the

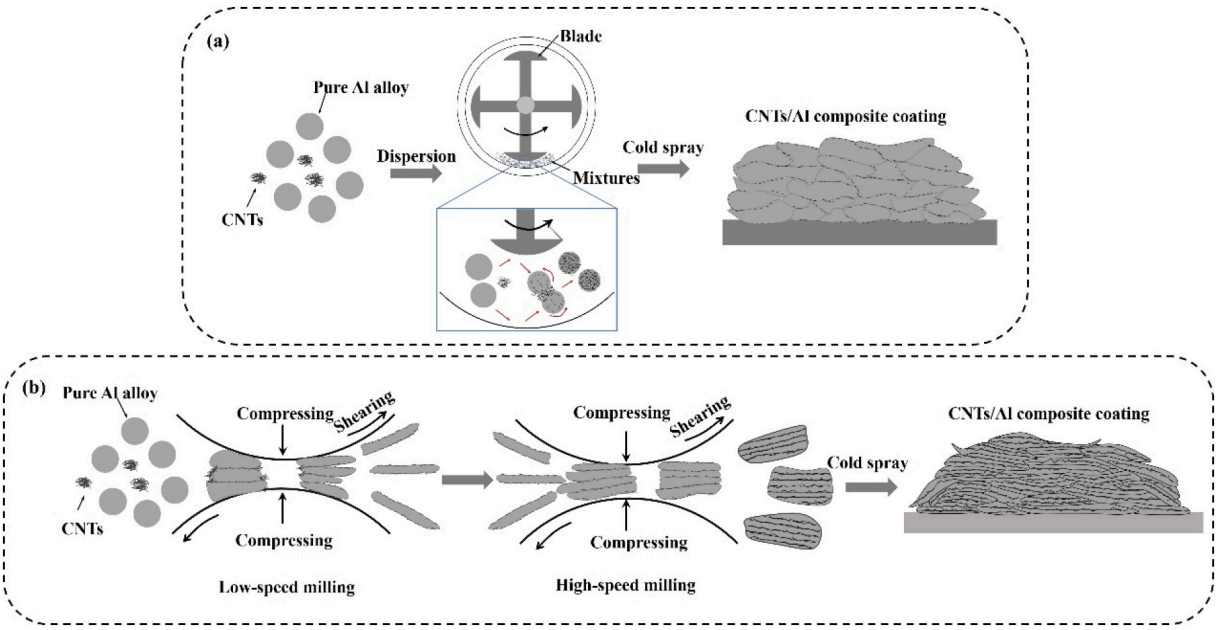

Fig. 1. Illustration of the (a) HSD process and (b) SSBM process for fabrication of the CNT/Al composite powder.

nozzle inlet. The initial particle velocity and temperature were set to 25 $m{\cdot}s^{-1}$ and 298 K, respectively. The densities of pure Al, HSD composite powder, and SSBM composite powder for the simulations were set to be 2.7 g/cm^3. As for the pure Al powder and HSD composite powder, a spherical shape and particle size of 25 μm were used for simulation based on the measurements of a laser diffraction sizer (Mastersizer 2000, Malvern Instruments Ltd., UK). In the case of SSBM composite powder, the influence of particle size and the shape factor on the particle velocity and particle temperature were investigated by CFD simulation.

2.4. Material characterization

In order to detect possible phase transformation during CS process, the as-sprayed coatings as well as the feedstock powders were examined by an X-ray diffractometer (XRD, Siemens D500, Germany) with the Co ($\lambda = 1.78897$ Å) source at a current of 40 mA, voltage of 35 kV and scan step of 0.02°. Raman spectroscopy tests were performed by using SENTERRA R200-L with the 532 nm line of an Ar^+ laser as the excitation source to validate the structure of CNTs and the formation of Al_4C_3 phase in the spectral range from 400 to 2000 cm^{-1}. Besides, Raman mapping of the cross-section of composite coatings was carried out to determine the CNTs distribution at a step size of 0.7 μm within an area of 30 × 30 μm^2.

The cross-sectional samples were prepared by standard mechanical polishing procedure. The morphology of the samples before and after etching (Keller's reagent) were observed using an optical microscope and a scanning electron microscope (SEM) (JSM5800LV, JEOL, Japan). To reveal the gain size of the different samples, electron back scatter diffraction (EBSD) characterization was performed using a SEM (JSM7800F, JOEF, Japan) equipped with an EBSD detector from Oxford instruments. As for EBSD measurements, an area of 118 × 95 μm^2 was recorded with a step size of 300 nm for the HSD coating, while an area of 30 × 30 μm^2 was recorded with a step size of 100 nm for the SSBM coating. Samples for EBSD mapping were prepared by mechanical polishing and final surface ion milling.

Adhesion strength of the deposits was evaluated based on the ASTM C-633 standard [31]. The composite coatings with an average thickness of around 300 μm were deposited on cylindric substrates with a diameter of 25.4 mm and a thickness of 10 mm. All substrates were grit blasted, cleaned in an ultrasonic bath of ethanol and were dried using compressed air prior to the CS. The roughness of the 316 stainless steel substrate after grit blasting has an average value of 19 μm. A tensile tester (IC ESCOFFIER, Estotest 50, France) was used to pull-out the adhesion samples at a speed of 1.26 mm/min. For each deposition condition, four adhesion samples were tested to obtain an average value. The coating microhardness was measured by a Vickers hardness indenter (Leitz, Germany) with a load of 100 g for 10 s. 10 positions were randomly tested to obtain an average $HV_{0.1}$ value.

3. Results and discussion

3.1. Powder morphology

Fig. 2 shows the morphologies of the initial feedstock powders. As can be seen from Fig. 2b, the shape of the HSD composite powders retained the nearly spherical shape as compared to the raw gas-atomized pure Al powder (see Fig. 2a). The magnified view of the HSD powder in Fig. 3b displays that the CNTs clusters were de-agglomerated and uniformly dispersed onto the surface of Al powder particles. The principle of dispersing CNTs onto Al particles by using the HSD process was similar to the dry particle coating process [32]. Firstly, with the collision between the Al particles and CNTs clusters in the container, CNTs clusters were de-agglomerated into smaller ones. Then these smaller CNTs were coated onto the surface of pure Al particles subjected to severe shear stress (see Fig. 1a). At last, uniform dispersion of CNTs spread over the Al particle surface was achieved by repeating collision between the Al particles.

Fig. 2c shows the morphology of the SSBM composite powders. Unlike the pure Al powder, the ball milled composite particles exhibit cake-like shape with sharp edges and flat surfaces. The cross-sectional view of a composite particle showed a clearly internal lamellar structure (Fig. 2f). The cake-like morphology and lamellar internal microstructure of the composite powder were attributed to the two opposing processes-the continual fracturing and cold welding. Different from the commonly used high energy ball milling process, a SSBM strategy i.e. 4 h starting low speed ball milling and 1 h following high-speed ball milling was used to fabricate the CNT/Al composite powder. As illustrated in Fig. 1b, the LSBM/4 h flattened the composite powder into nano-flakes, meanwhile CNTs uniformly dispersed on their surface. Then nano-flakes could be cold welded into lamellar structured particles during the short

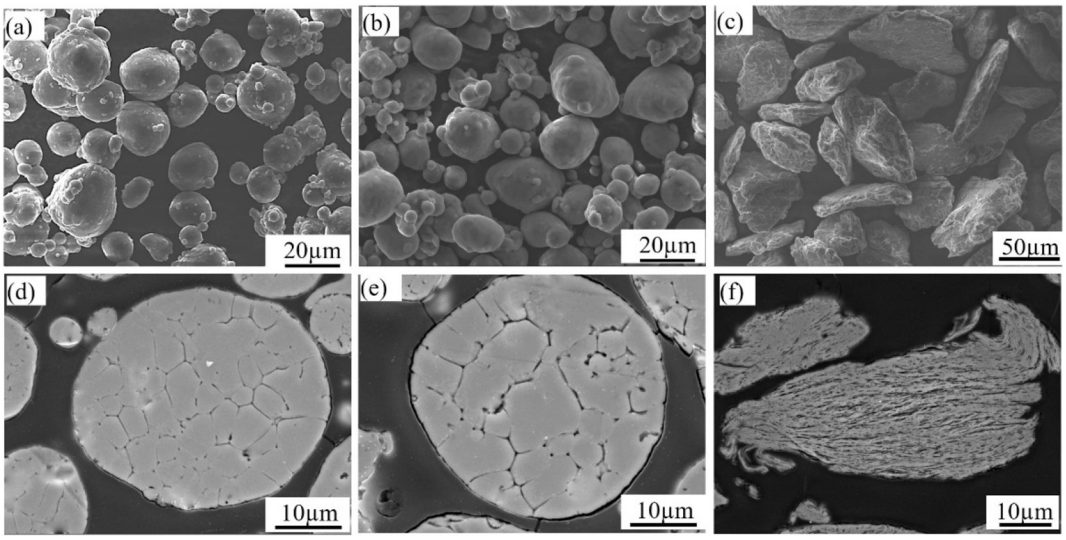

Fig. 2. SEM images showing surface morphologies and cross-sectional views of the feedstock powders: (a) and (d) pure Al powder; (b) and (e) HSD CNT/Al composite powder; (c) and (f) SSBM CNT/Al composite powder.

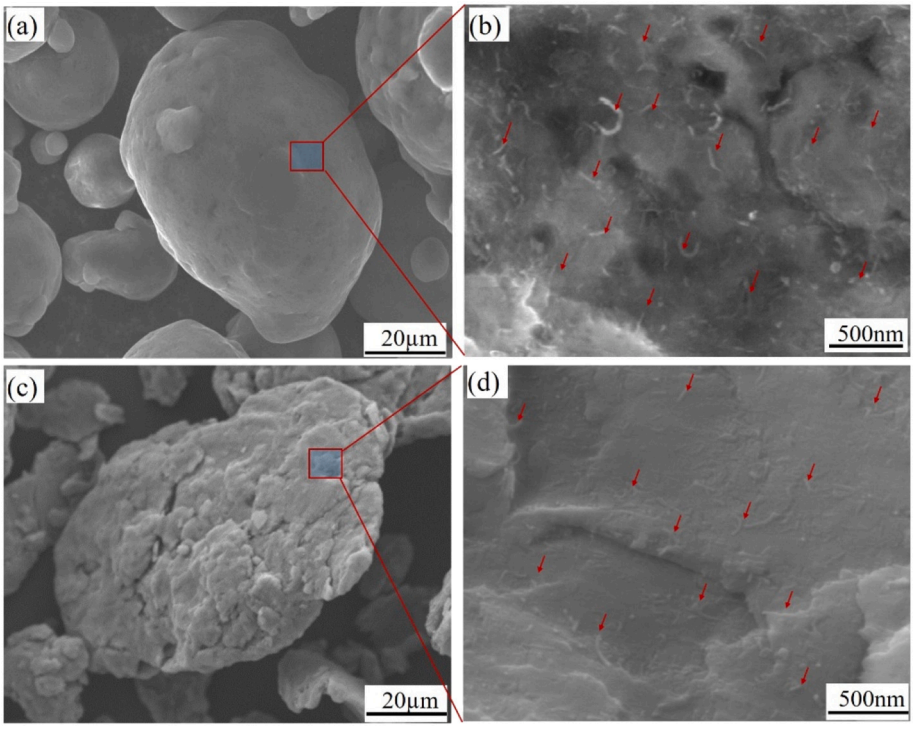

Fig. 3. SEM images showing CNT distributions in the composite powder particles processed by (a, b) HSD and (c, d) SSBM methods.

HSBM process. Therefore, the coordination of CNTs dispersion, integrity and interfacial bonding could be achieved by using such a special designed strategy [15]. As can be seen from Fig. 3d, CNTs were uniformly dispersed on the surface of the flaky composite particles.

As shown in Fig. 4, the HSD composite powder exhibits the similar particle size distribution compared with the pure Al powders, having an average particle size of ~25 μm. The SSBM composite powder has an average particle size of ~62 μm due to the flattening and welding effect.

3.2. Particle impact velocity and temperature

Based on CFD simulation, the pure Al particle velocity and particle temperature along the nozzle central line are given in Fig. 5. Fig. 6 presents the particle impact velocity and temperature as a function of propelling gas temperature (300–550 °C). Clearly, both the particle impact velocity and temperature increase with the increase of propelling gas temperature. A particle impact velocity of 642 m/s and a particle impact temperature of 355 °C were obtained at a propulsive gas (compressed air) pressure of 3.0 MPa and a temperature of 550 °C. It should be noticed that the HSD CNT/Al composite powder could have similar particle impact velocity and temperature compared to the pure Al powder as they have similar particle size, morphology and other physical properties, including density and specific heat.

In addition, the SSBM CNT/Al composite powder after ball milling displayed a non-spherical morphology. This can also affect the acceleration behavior of the particle within the nozzle. Therefore, a variation of

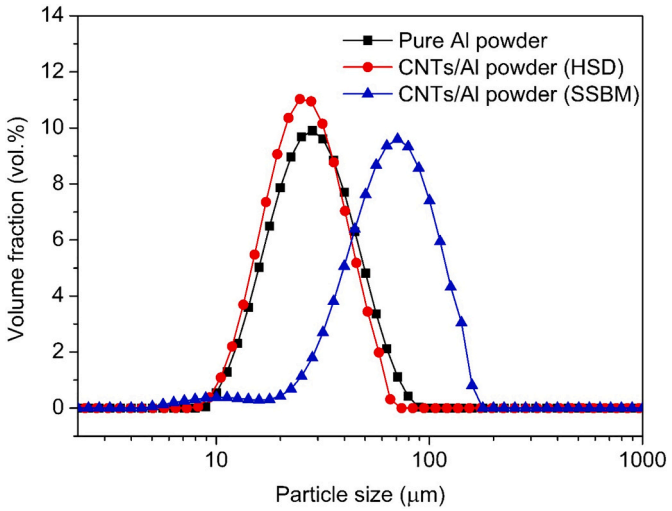

Fig. 4. Particle size distributions of the different powder feedstocks.

shape factor from 0.3 to 1 was considered for the Al particles. The particles with three equivalent diameters of 25, 45 and 62 μm were used for simulation (gas pressure of 3.0 MPa and temperature of 550 °C), and the results are given in Fig. 7. A smaller shape factor (i.e., $\Psi_{Wa} = 0.6$) exhibits greater particle velocities as a result of drag force. Further, it was found that smaller equivalent diameters reduced the effect of the shape on the velocity. In addition, the temperature of the non-spherical particles was slightly greater over the complete distance up to impact than that of the spherical particles.

3.3. Deposition efficiency

Fig. 8 a shows the DEs of the pure Al and CNT/Al composite feedstocks obtained using the different CS processing conditions. As the propelling gas temperatures increased from 300 to 550 °C, the DE of each feedstock increased gradually. The DEs of both CNT/Al composite powders were much lower than the pure Al powder using the same processing conditions. Besides, the SSBM composite powder possesses a lower DE value compared to the HSD composite powder. The evolution of DEs resulted from the gap between the mean particle velocity and the critical velocity. From the point of view of CS, the enhanced DE with the propelling gas temperature increased from 300 to 550 °C was due to improved mean particle velocity relative to the critical velocity (see Fig. 6). Besides, an increase in the inlet gas temperature, which also increases the particle impact temperature and the DE (see Fig. 6).

Due to the similar size distribution and surface morphology, the HSD composite powder and pure Al powder should have similar impact velocity and resulting DE values under the same processing parameters. Therefore, in terms of the HSD composite powder, the primary cause of the decrease in DE was the strengthening effect by embedded CNTs covering the particle surface. It has been well-known that the critical velocity of a feedstock material can be affected by its mechanical properties of the material (i.e. deformability of material) [33]. Besides, the critical velocity and DE were also found to be connected with the particle surface contamination level [34,35]. Also, the contamination-free interface is of great importance for the true metal-to-metal contact and the successful particle-substrate or interparticle metallic bonding [36]. Therefore, the dispersion of CNTs on the surface of particles may play an equivalent role like oxide films, that can prevent the impact particles from metallic bonding. As the surface morphology of pure Al coating is given in Fig. 9a and b, the seriously deformed particles can be observed. As for the HSD coating, obvious traces of rebounded particles can be noticed on the surface, indicating the unsuccessful bonding and rebounding off due to the limited particle deformation. Consequently, the HSD composite powder decorated with CNTs showed a much lower DE compared to pure Al powder.

In terms of SSBM composite powders, apart from the two reasons above mentioned, the work hardening effect and grain refinement

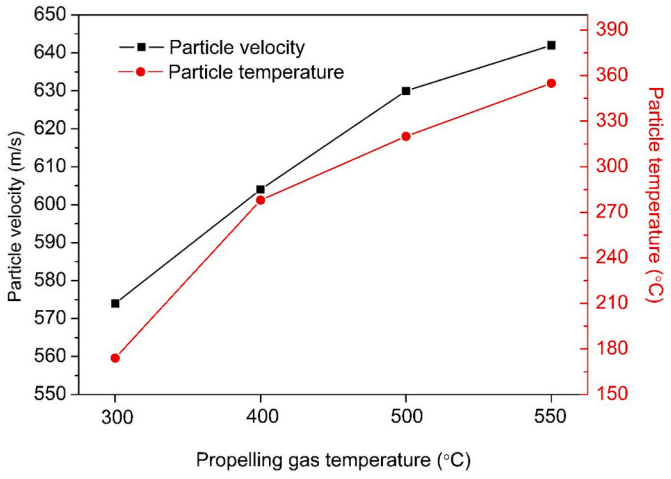

Fig. 6. Particle impact velocity and temperature as a function of propelling gas temperature.

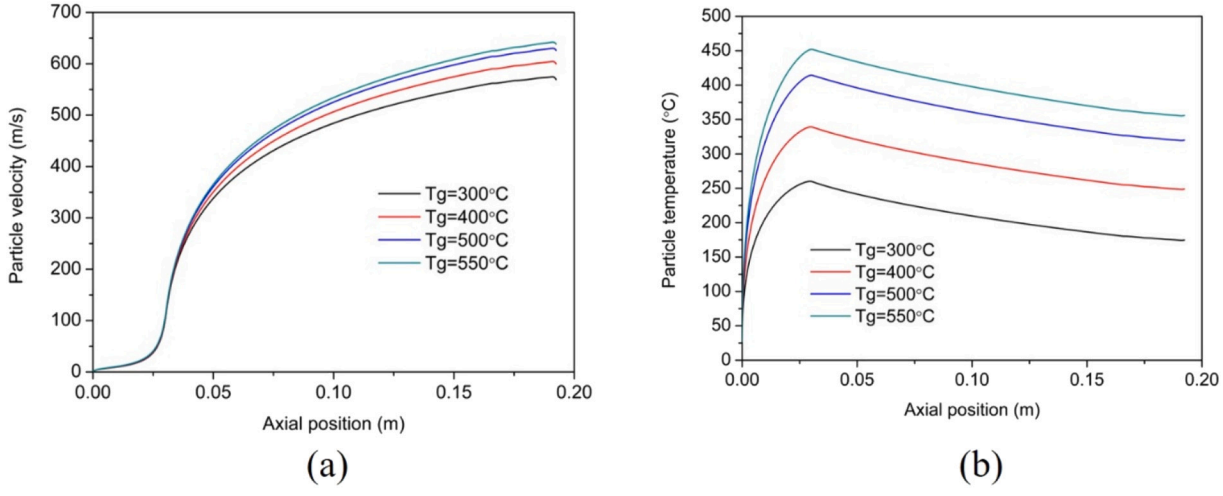

Fig. 5. (a) Particle velocity and (b) particle temperature along the nozzle central line.

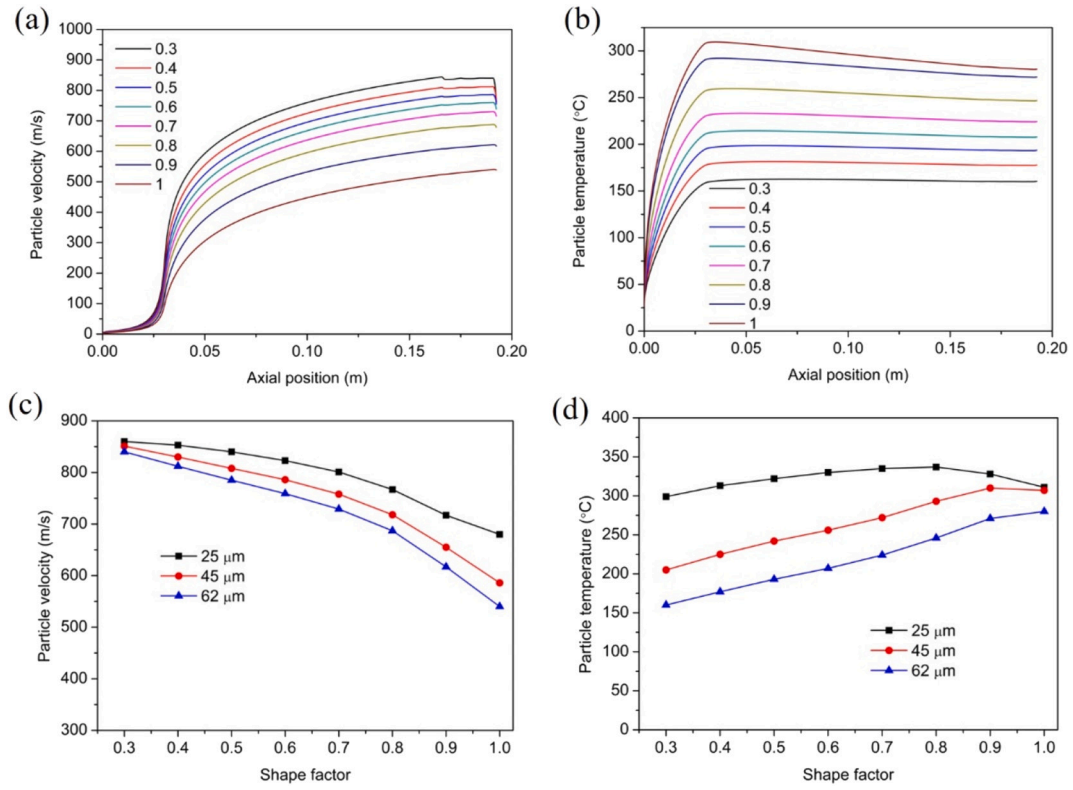

Fig. 7. (a) Particle velocity and (b) particle temperature along the nozzle central line for the particles with the shape factor from 0.3 to 1; (c) and (d) show particle impact velocity and particle impact temperature as a function of shape factor, respectively. Equivalent average particle sizes of 25 μm and 45 μm and 62 μm were used for this simulation.

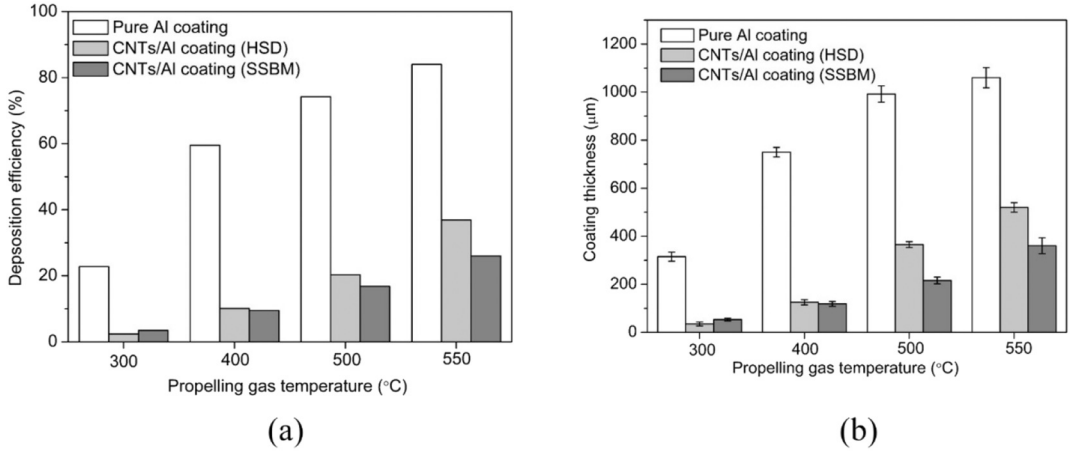

Fig. 8. (a) DE and (b) coating thickness as a function of propelling gas temperatures.

during ball milling process may be the main factors leading to the decrease of DE. The increased hardness of powder particles after ball milling is unfavorable for CS deposition, as harder particles require a higher critical velocity [37]. As shown in Fig. 9e, many traces of rebounded particles in the coating surface can be observed. These rebounded particles were acted as in-situ shot peening particles, inducing hammering effect on the previous deposited layers.

3.4. Coating microstructure

Fig. 10 shows the optical micrograph of the cold sprayed pure Al and CNT/Al composite coatings at the different propelling gas temperatures. It can be seen that the coating thickness increases with the increase of propelling gas temperature. As for different feedstock particles, thick and dense coatings were formed at higher gas temperatures, indicating the increasing DE values. Compared with the pure Al coating, much lower thickness values were obtained in both HSD and SSBM composite coatings. The evolution of coating thickness values is shown in Fig. 8b. Etched cross-sectional images of coatings deposited at 550 °C are shown in Fig. 11. As can be seen from Fig. 11a and d, the deposited pure Al particles were severely deformed, forming a parachute shape and intimate inter-particle bonding. The grains at inter-particle boundaries were severely elongated due to strain localization during CS. The HSD composite coating, however, contained voids as indicated by the arrows in images (Fig. 11b and e). These voids appeared to be gaps along the particle boundaries. This result suggests that the dispersion of CNTs onto

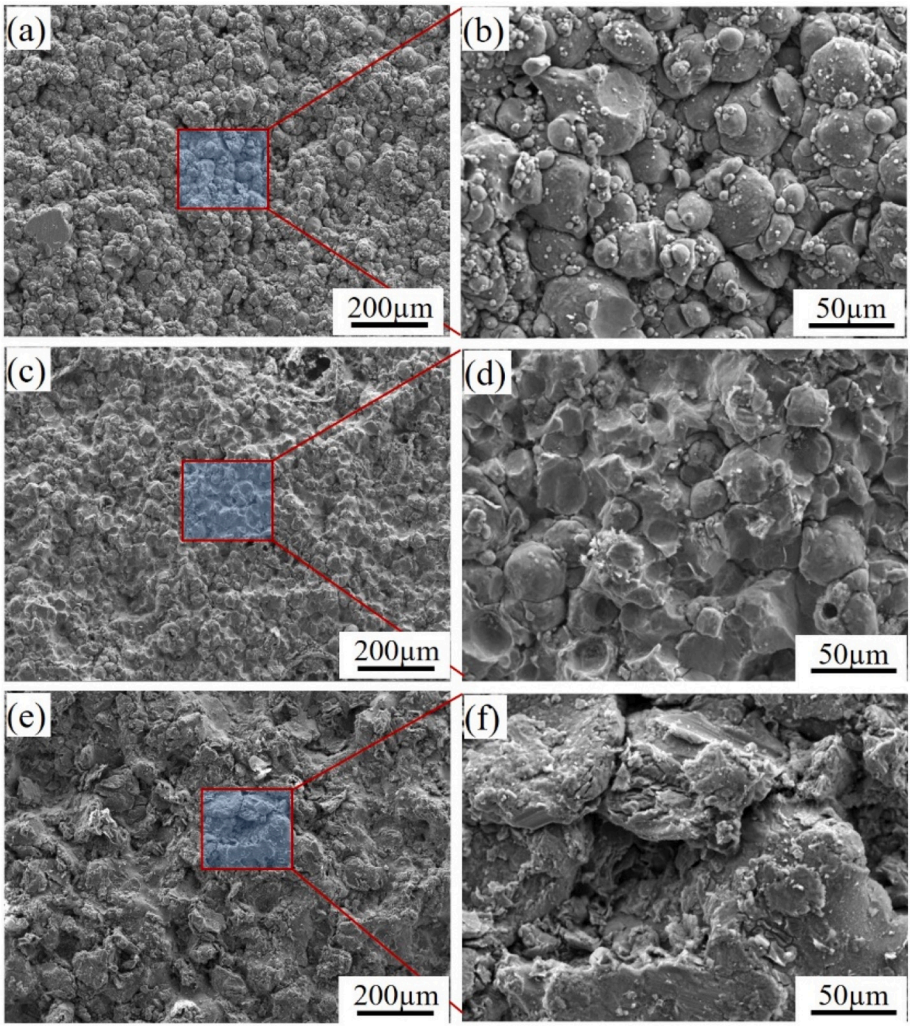

Fig. 9. SEM images showing surface morphologies of the coatings produced from (a) pure Al powder, (c) HSD composite powder and (e) SSBM composite powder.

the particle surface can affect the metallic bonding of the particles during coating built-up. As the processing gas temperature decreased from 550 to 500 °C, interestingly, the CNT/Al particles experienced greater plastic deformation (Fig. 12a and c). As the propelling gas temperature decreased further to 400 °C, a "curly" structure with enhanced bonding of largely deformed particles was formed (Fig. 12b and d). This observed microstructure evolution is not consistent with the existing concept of the relationship between velocity and particle deformation during CS deposition, where a higher particle impact velocity results in a greater particle deformation. The peening effect should be responsible for the enhanced particle deformation at lower processing parameters. A lower DE at low propelling gas temperature leads to a stronger in-situ particle peening effect of the rebounding particles. As a result, the previous deposit undergoes greater deformation with the aid of such enhanced in-situ hammering effect [38,39]. It should be noticed that such a trend was not observed in pure Al coating due to a much lower peening effect during the deposition of pure Al particles.

Very different from the pure Al coating and HSD composite coating, the microstructure of the SSBM composite coating exhibits a wavy shape with intimate inter-particle bonding states (Fig. 11c and f). This is influenced by the cake-like shape of the initial composite particle. The lamellar structure of the initial composite powder was well retained in the composite coating. Since the grains of the initial composite particle were sub-micron or even smaller, grain boundaries were not revealed even after chemical etching. Besides, inter-particle boundaries were also difficult to identify.

EBSD characterization was applied to further investigate the particle deformation behavior and microstructure of the cold sprayed CNT/Al composite coatings produced from the two different feedstocks. As shown in the Euler angle maps (see Fig. 13a and b), significant difference in microstructure between these two composite coatings can be observed. As for the HSD composite coating (see Fig. 13a), the particle deformation was clearly inhomogeneous, as shown by the mixture of large grains and equiaxed small grains. The particle-particle boundary regions, where particles experienced severe deformation during deposition, were characterized by ultrafine grain structure. Particle interiors were characterized by large grains. According to the grain size distribution map (see Fig. 13c), the average grain size of this composite coating was measured to be about 1.2 μm. Furthermore, a relatively high quality is seen in this Euler angle map, indicating low defect density and lattice strain. As for the SSBM coating (see Fig. 13b), ultrafine grains were uniformly distributed, showing great difference in microstructure from the HSD coating (see Fig. 13a). The average grain size of this composite coating was measured to be 215 nm (see Fig. 13d). The indexation rate of this composite coating was much lower than that of HSD coating. This indicated that there was relatively high defect density and/or lattice strain inside the ultrafine grains, which was mainly formed during the SSBM process. Therefore, the powder preparation approach has a significant influence on the microstructure of composite powder, which later was well-retained in the composite coating.

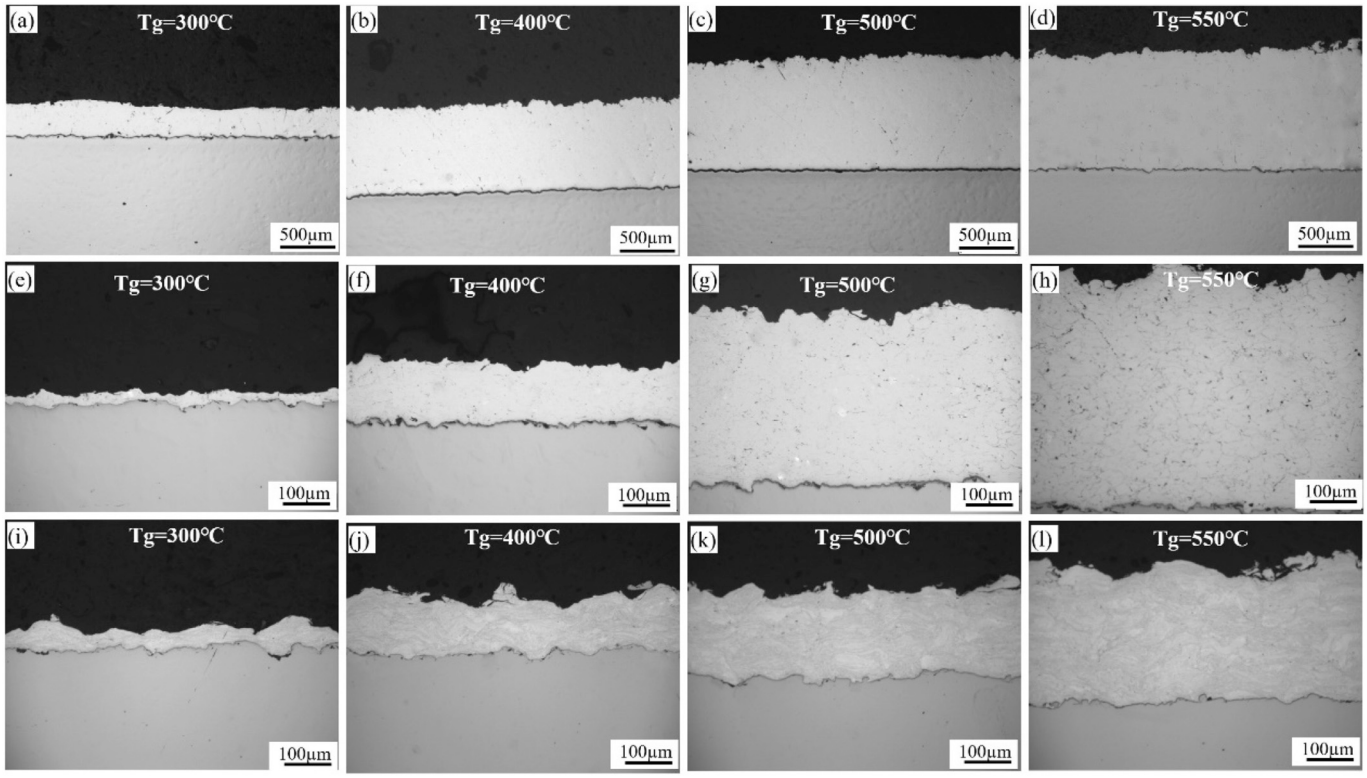

Fig. 10. Optical micrographs of the coatings produced using the different feedstocks at the different propelling gas temperatures: (a–d) pure Al coating; (e–h) HSD composite coating; (i–l) SSBM composite coating.

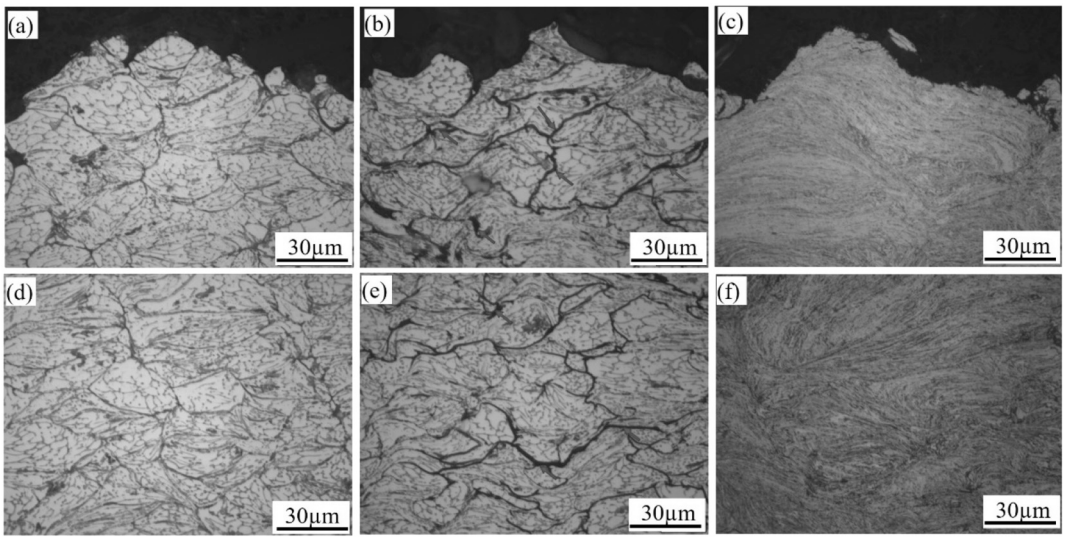

Fig. 11. Optical micrographs showing etched cross-sectional microstructures of the coatings deposited with different feedstocks at the processing gas temperature of 550 °C: (a) and (d) pure Al coaying; (b) and (e) HSD composite coating; (c) and (f) SSBM composite coating. (a–c) Top areas and (d–f) center areas of the corresponding coatings. The red arrows in (b) and (e) indicate inter-splat interface. (For interpretation of the references to color in this figure legend, the reader is referred to the web version of this article.)

3.5. Distribution and structure integrity of CNTs

The XRD patterns and Raman spectra of the as-processed materials are shown in Figs. 14 and 16, respectively. No obvious peaks corresponding to brittle Al_4C_3 phase can be observed from the XRD patterns (the main Al_4C_3 peak is at ~55° [40]) and Raman analysis (main peak is at ~850 cm^{-1} [41]) even though the high gas temperature of 550 °C was used, which is frequently observed in the CNT/Al composites made by powder metallurgy [15]. This should be attributed to the low particle impact temperature feature of CS.

Due to the relatively low content (1.5 wt%) and size of CNTs in the Al matrix, SEM/EDS is incapable of determining their distributions in the composite coatings. According to previous studies [42–44], the Raman spectra provides an exceedingly powerful tool for the characterization of CNTs, as it can reveal the characteristic G-band, indicating high crystalline graphite layers of CNTs. Therefore, Raman mapping of the cross-

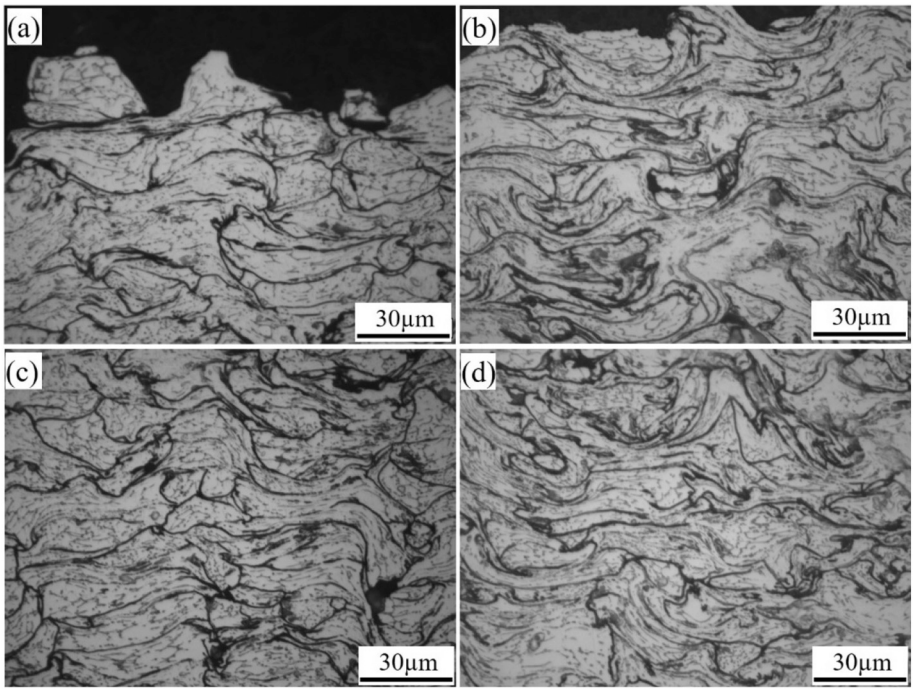

Fig. 12. Optical micrographs showing etched cross-sectional microstructures of the CNT/Al HSD composite coatings fabricated at processing gas temperature of (a, c) 500 °C and (b, d) 400 °C. (a, c) Top areas and (b, d) center areas of the corresponding coatings.

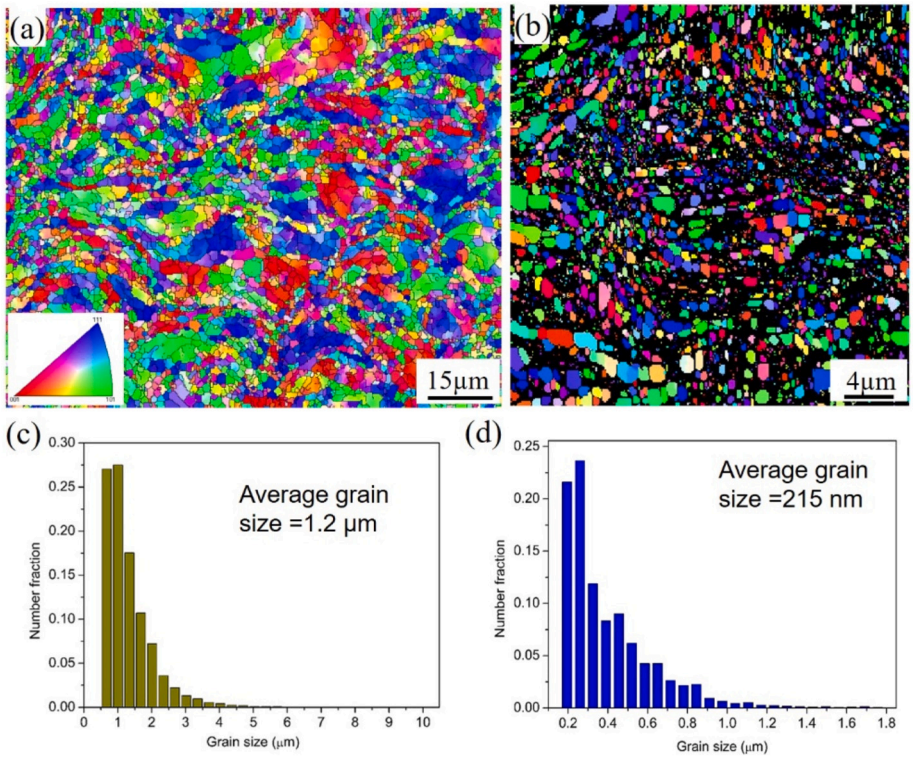

Fig. 13. Cross-sectional EBSD characterization of the as-sprayed composite coatings at the propelling gas temperature of 550 °C: (a) Euler angle map and (c) grain size distribution of HSD composite coating; (b) Euler angle map and (d) grain size distribution of SSBM coating.

section of composite coating was carried out to determine the distribution of CNTs. The corresponding confocal Raman mapping images highlighting the intensity of G-band (1520– 1650 cm^{-1}) of the HSD coating and SSBM coating are shown in Fig. 15b and e, respectively. The green color indicates the presence of CNTs. In the case of HSD composite coating (Fig. 15b), one can notice that CNTs are mainly concentrated around the particle boundaries rather than within the particles. In the case of SSBM coating (Fig. 15e), CNTs are uniformly distributed over the entire region (30 × 30 μm^2) without detectable agglomeration. These results suggest the uniform distribution of CNTs by SSBM processing,

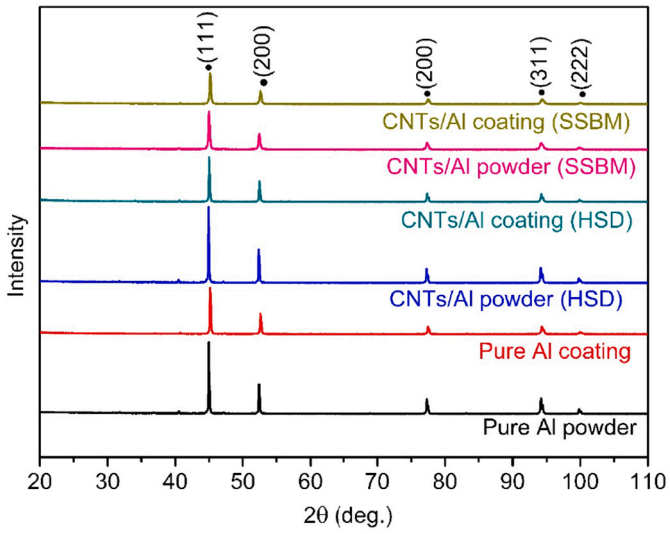

Fig. 14. XRD patterns of cold sprayed coatings and feedstock powders.

while the HSD process failed in dispersion of CNTs inside the Al particles.

In addition, Raman spectroscopy was used to characterize the structural integrity of CNTs. As shown in Fig. 16, the peaks at ~1350 cm^{-1} and ~1570 cm^{-1} correspond to a typical D-band and G-band, respectively [42]. Generally, the G-band reveals highly crystalline graphite layers, and the D-band reveals the presence of defects in the graphite layer [42]. Therefore, intensity ratio (I_D/I_G) is capable of providing information on the crystal structure of CNTs [10,45]. Thus, a higher value of intensity ratio (I_D/I_G) indicates greater damage of CNTs structure. The average I_D/I_G value of the HSD powder was measured to be ~1.26, showing a slight increment compared with the raw CNTs powder (1.22). This result suggests that the structural integrity of CNTs was well retained during the HSD process. Comparatively, the I_D/I_G value of the HSD coating increased from 1.26 to 1.44, indicating some structural damages of CNTs during CS process. Fig. 15c shows the map of I_D/I_G values in the HSD composite coating. The high I_D/I_G values can be found inter-particles. Also, the I_D/I_G value of SSBM powders increased to 1.35, indicating that the CNTs were slightly damaged during SSBM processing. Comparing with the popularly used high-speed ball milling process, the dispersion method used in this study (SSBM) showed less structural damages of CNTs because of the relatively low energy input [15]. After CS deposition, the I_D/I_G value slightly increased from 1.35 to 1.40. Therefore, less structural damages of CNTs were found during the deposition of ball milled composite powder compared with the CNTs coated composite powder. Besides, a peak shift of G-band from ~1570 to ~1590 cm^{-1} was observed in the CNT/Al composites. The peak shift might originate from the infiltration of Al atoms in CNTs, causing slight distortion of sp^2 bonding structure of CNTs [5,46].

In the case of HSD composite coating, since CNTs were distributed on the surface of Al particles, they could be shortened in length and fractured due to the impact and shearing between composite particles

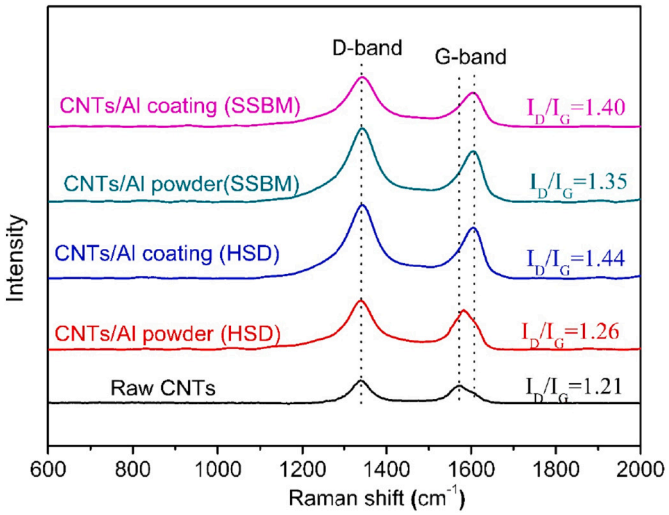

Fig. 16. Raman spectra of the feedstocks and composite coatings.

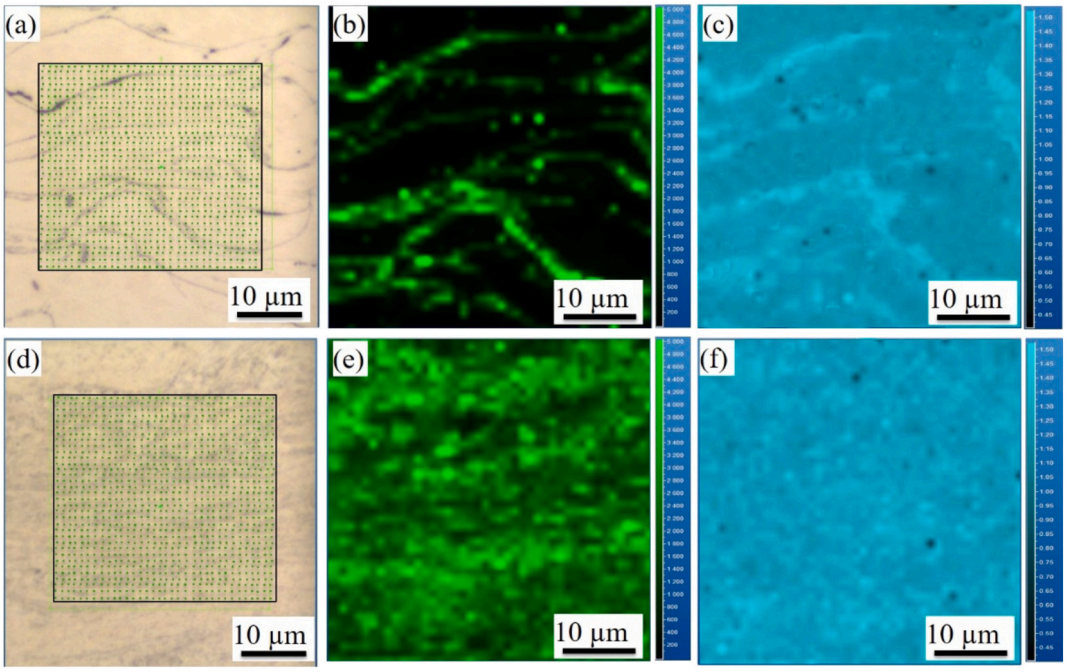

Fig. 15. Raman spectra mapping of the (a–c) HSD coating and (d–f) SSBM coating fabricated at 550 °C: (a) and (d) Optical micrographs; (b) and (e) Corresponding confocal Raman maps of G-band intensity (1520– 1650 cm^{-1}); (c) and (f) Maps of I_D/I_G ratio value.

during the deposition process. In the case of SSBM composite coating, some structural damages of CNTs were found during the SSBM process while less damage occurred during the deposition process. This is because the SSBM process allows uniform distribution of CNTs inside the Al particles, which can prevent most of the CNTs from being fractured during deposition process, due to severe plastic deformation mainly occurred at the rim of the composite particles. The structural integrity of CNTs could have significant influence on mechanical properties of the CNT/Al composites. This part of work will be carried out in the future.

3.6. Adhesion strength

Tensile pull-off adhesion testing was conducted to investigate the influence of powder type and CS processing conditions on the resulting coating adhesion strength. Fig. 17 provides the adhesion strength values of the pure Al, HSD and SSBM composite coatings deposited on the SS substrates at the different gas temperatures (the absence of the adhesion strength values of the HSD and SSBM composite coatings at 300 °C is because of their too thin coatings for this test). It is evident that the pure Al coating possesses much higher adhesion strength compared to both HSD and SSBM composite coatings. Besides, the adhesion strength of the pure Al coating increases with the increase of propelling gas temperature, and the highest value of ~37 MPa is obtained at 550 °C. However, the adhesion strength of the HSD composite coating experienced a small decrease when adjusting the gas temperature from 400 to 550 °C. The adhesion strength of the SSBM composite coating shows little variation at different processing temperatures.

The adhesion strength is mainly determined by mechanical (including the plastic deformation of particle and substrate) and thermal interaction between particle and substrate when the particles impact onto substrate with a high velocity [47,48]. Previous studies found that the particle impact velocity, particle or substrate temperature, substrate roughness, particle morphology as well as mechanical properties of the particle and substrate play important roles in evaluating adhesion strength based on plastic deformation [48,49]. A higher particle velocity at a higher gas temperature benefits the mechanical interlock effect resulting in excellent bonding between the coating and substrate. In addition, particles sprayed with higher gas temperatures are expected to retain some thermal energy and arrive at the substrate at a higher temperature than those with lower gas temperatures. Such an increased temperature can reduce the shear stress of Al and can affect the deformation and adhesion mechanisms of the material [50]. Therefore, a higher adhesions strength of the pure Al coating was achieved at a higher gas temperature.

The HSD composite coatings showed much lower adhesion strength values than those of the pure Al coatings. The presence of CNTs around the Al particles, on the one hand, can act as impurities which can prevent the exposure of fresh metal and metallic bonding of the composite particle and substrate; on the other hand, the enhanced work hardening of CNTs can prevent plastic deformation of the particles to form adiabatic shear instability between the particle and the substrate. These factors lead to the lowed adhesion strength in comparation with the pure Al powder. The slight increasement of adhesion strength at a lower gas temperature can be explained by the enhanced in-situ hammering effect, which can lead to greater particle deformation and improved mechanical interlocking of the composite particles into the substrate.

In the case of SSBM composite coating, even though the particle with irregular shape may possess a higher particle impact velocity due to its better acceleration aspect in the gas flow (see Fig. 7), the enhanced work hardening effect resulted from balling milling and CNTs dispersion can lead to a much higher critical velocity for successful deposition. Further, as addressed by the FEA simulation result from S.Yin et al. [51], quite a small fraction of interface can realize the true metallic bonding for the irregular particle due to the very limited particle deformation. As a result, the cake-like particle can result in worse bonding between the substrate in comparation with the spherical particles.

3.7. Coating microhardness and strengthening mechanisms

The measured microhardness values of pure Al and the composite coatings as a function of processing gas temperatures are shown in Fig. 18. The microhardness of the as-sprayed pure Al coating gradually increased from 36 to 50 $HV_{0.1}$ as the processing gas temperature increased from 300 to 550 °C. This is because higher particle impact velocity can be achieved at the high processing parameters, which leads to the enhanced particle deformation to form fully dense coatings. The microhardness of the 1.5 wt% CNT/Al composite coating produced from HSD powder showed a slight increment at the low propelling gas temperatures compared with the pure Al coating. As the propelling gas temperature increased, its microhardness slightly decreased, even lower than that of pure Al coating at the same processing parameters. These results demonstrate that the dispersion of CNTs by HSD approach did not achieve significant strengthening effect on the composite coatings, but adversely affect the metallic bonding of the particles, resulting in decreased strength. The CNT/Al composite coating produced from the SSBM powder had a value of 115 $HV_{0.1}$, which was more than twice that

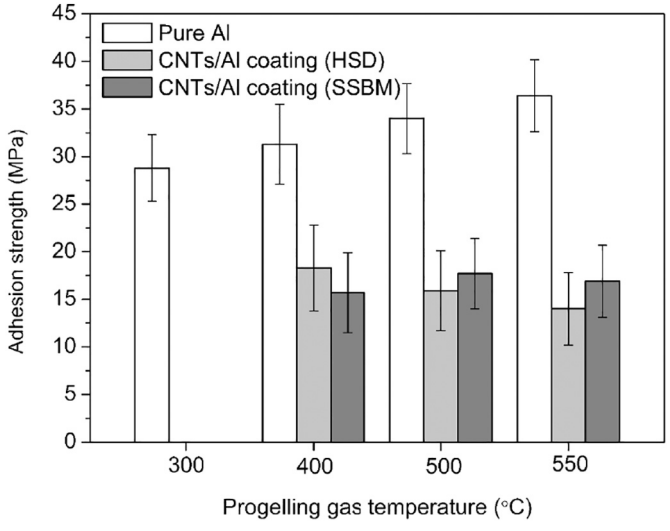

Fig. 17. Adhesion strength values of the pure Al, HSD composite and BBSM composite coatings deposited on stainless steel substrate at the different propelling gas temperatures.

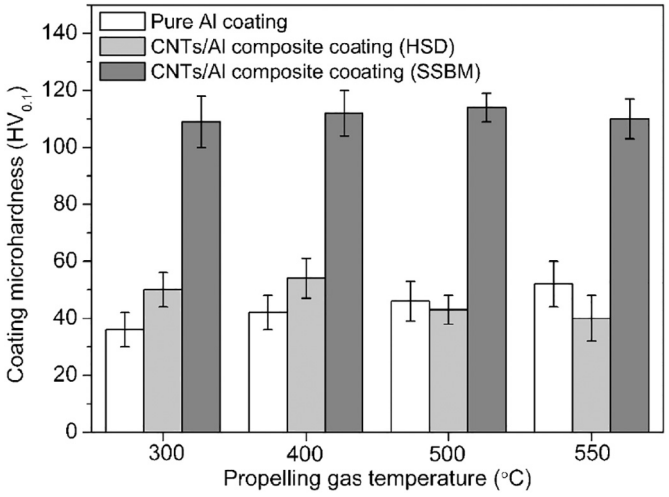

Fig. 18. Microhardness of the as-sprayed coatings at different propelling gas temperatures.

of the pure Al coating. Meanwhile, no significant difference in the microhardness of the CNT/Al composite coatings was found at the different propelling gas temperatures. One important reason for the significant improvement in strength is that fully dense microstructure was achieved in these SSBM composite coatings.

The strengthening mechanisms of the cold sprayed CNT/Al composite coatings are related to the microstructure. The microhardness of the cold sprayed composites can be expressed as follows [27]:

$$H = H_0 + \Delta H_{WH} + \Delta H_{GB} + \Delta H_{CNTs} \quad (2)$$

where H_0 is the microhardness of annealed Al with coarse grains (15.0 $HV_{0.1}$), ΔH_{WH} is the strengthening due to work hardening, the strength contribution of the grain boundary (Hall-Petch relation), and ΔH_{CNTs} hardening by the dispersion of CNTs into Al matrix. The work hardening is expressed as follows [52]:

$$\Delta H_{WH} = k_w \rho_{dis}^{1/2} = \alpha G b \rho_{dis}^{1/2} \quad (3)$$

Here, G is the shear modulus of Al, b is the Burgers vector, α is a constant (0.3), and $\rho_{dis}^{1/2}$ is the dislocation density of the grain interior. The dislocation density of a kinetic sprayed Al coating was reported to be $\sim 10^{11}$ cm^{-2} [53]. Since the plastic deformation of the HSD composite powder was similar with the pure Al powder, the dislocation density in the HSD composite coating should have a magnitude equal to that of pure Al coating. Therefore, the calculated work hardening effect of the cold sprayed HSD composite coating was 27.9 $HV_{0.1}$ (256.1 MPa), which was consistent with the value of pure Al coating in Ref [28]. As for the SSBM composite coating, the work hardening effect resulted from SSBM powder preparation process was more pronounced than that from the CS process. This is because a large grain boundary area of the nanosized Al matrix accommodated the dislocations during the CS deposition [28,52].

The grain boundary hardening (Hall-Petch relation) can be expressed as follows:

$$\Delta H_{HP} = k_H d^{-1/2} \quad (4)$$

where k_H (0.14 MPa $m^{1/2}$) is constant, and d is the grain diameter. In this work, the grain size of the cold sprayed HSD composite coating was similar with that of pure Al coating, which was measured to be 1.2 μm (Fig. 13c). The calculated grain boundary hardening of the HSD coating was 13.9 $HV_{0.1}$ (127.8 MPa). Since the average grain size of the cold sprayed SSBM composite was measured to be 215 nm (Fig. 13d), the grain boundary hardening of the SSBM composite coating was 32.8 $HV_{0.1}$ (302 MPa). These results indicate that greater grain boundary hardening effect was achieved in the SSBM composite coating due to its ultra-fine microstructure.

The hardening by CNTs embedded in the Al matrix was attributed to Orowan looping by CNTs [45]. The stiff CNTs in the ductile Al matrix act as barriers to dislocation movement. As a result, pile-ups of the dislocations occurred, enhancing hardening of the Al matrix around the CNTs. Hardening by CNTs can be expressed as follows [27,45]:

$$\Delta H_{CNTs} = \frac{0.13 G b}{\lambda} ln(2r/r_0) \quad (5)$$

where r is the volume equivalent radius of a CNT (1.593×10^{-7} m) [28], r_0 is the core radius of a dislocation (3.5×10^{-9} m) and λ is the distance between CNTs. In the case of HSD composite coating, since the CNTs were mainly distributed along the inter-particle boundaries, and obvious gap between CNTs and Al matrix can be observed (see Fig. 12b), the strengthening effect by CNTs was largely weakened. In the case of the SSBM composite, the CNTs were uniformly distributed into the Al matrix, resulting in the significant improvement in strength because of the Orowan looping by CNTs in the composite. Detailed investigation of the interface between CNTs and Al matrix of the cold sprayed composites will be carried out by transmission electron microscopy.

4. Conclusions

In this work, both HSD and SSBM composite CNT/Al powders were used as the feedstocks to fabricate CNT/Al composite coatings by CS deposition. In the case of HSD composite, CNTs were uniformly dispersed on the surface of Al particles without serious damages of CNTs. However, the dispersion of CNTs onto the Al particle surface could prevent the particles from metallic bonding during CS deposition, resulting in dramatic decrease of DE and low adhesion strength of the composite coating. Comparatively, in the case of SSBM composite, the uniform distribution of CNTs into Al matrix was achieved and the CNTs were slightly damaged during processing. The microhardness of the CNT/Al composite coating produced from SSBM powders reached 115 $HV_{0.1}$, showing a significant improvement compared with the pure Al coating. The strengthening mainly resulted from grain boundary hardening due to nanocrystalline structure and hardening by CNTs. In addition, according to the XRD and Raman analyses, the brittle Al_4C_3 phase was not formed in both CNT/Al composite coatings.

CRediT authorship contribution statement

Xinliang Xie: Methodology, Writing – original draft. **Zhanqiu Tan:** Methodology, Investigation. **Chaoyue Chen:** Methodology, Conceptualization. **Yingchun Xie:** Methodology, Investigation. **Hongjian Wu:** Methodology. **Xingchen Yan:** Methodology, Investigation. **Shuohong Gao:** Methodology. **Zhiqiang Li:** Investigation, Conceptualization. **Gang Ji:** Supervision, Writing – review & editing. **Hanlin Liao:** Conceptualization, Supervision, Project administration.

Declaration of competing interest

The authors declared that there is no interest conflict in this work.

Acknowledgments

Xinliang XIE thanks the financial support from the program of China Scholarship Council (No. 201604490100), Université Bourgogne Franche-Comté, and Centre National de la Recherche Scientifique (CNRS). The authors would like to thank Xi Chen and Prof. Cecile Langlade from ICB-LERMPS for the Raman measurements. The microscopy facility in Lille, France, is supported by the Conseil Regional du Nord-Pas de Calais and the European Regional Development Fund (ERDF).

References

[1] William A. Curtin, Brian W. Sheldon, CNT-reinforced ceramics and metals, Mater. Today 7 (2004) 44–49.
[2] Valentin N. Popov, Carbon nanotubes: properties and application, Mater. Sci. Eng. R 43 (2004) 61–102.
[3] Srinivasa R. Bakshi, Arvind Agarwal, An analysis of the factors affecting strengthening in carbon nanotube reinforced aluminum composites, Carbon 49 (2011) 533–544.
[4] B. Chen, J. Shen, X. Ye, H. Imai, J. Umeda, M. Takahashi, K. Kondoh, Solid-state interfacial reaction and load transfer efficiency in carbon nanotubes (CNTs)-reinforced aluminum matrix composites, Carbon 114 (2017) 198–208.
[5] B. Chen, K. Kondoh, H. Imai, J. Umeda, M. Takahashi, Simultaneously enhancing strength and ductility of carbon nanotube/aluminum composites by improving bonding conditions, Scr. Mater. 113 (2016) 158–162.
[6] Toru Noguchi, Akira Magario, Shigeru Fukazawa, Shuichi Shimizu, Junichi Beppu, Masayuki Seki, Carbon nanotube/aluminium composites with uniform dispersion, Mater. Trans. 45 (2004) 602–604.
[7] Hansang Kwon, Mehdi Estili, Kenta Takagi, Takamichi Miyazaki, Akira Kawasaki, Combination of hot extrusion and spark plasma sintering for producing carbon nanotube reinforced aluminum matrix composites, Carbon 47 (2009) 570–577.
[8] A. Esawi, K. Morsi, Dispersion of carbon nanotubes (CNTs) in aluminum powder, Compos. Part A 38 (2007) 646–650.
[9] Amal M.K. Esawi, K. Morsi, A. Sayed, A. Abdel Gawad, P. Borah, Fabrication and properties of dispersed carbon nanotube–aluminum composites, Mater. Sci. Eng. A 508 (2009) 167–173.
[10] Chunnian He, Naiqin Zhao, Chunsheng Shi, Xiwen Du, Jiajun Li, Haipeng Li, Qingran Cui, An approach to obtaining homogeneously dispersed carbon

nanotubes in Al powders for preparing reinforced Al-matrix composites, Adv. Mater. 19 (2007) 1128–1132.
[11] Lin Jiang, Zhiqiang Li, Genlian Fan, Linlin Cao, Di Zhang, The use of flake powder metallurgy to produce carbon nanotube (CNT)/aluminum composites with a homogenous CNT distribution, Carbon 50 (2012) 1993–1998.
[12] Zan Li, Qiang Guo, Zhiqiang Li, Genlian Fan, Ding-Bang Xiong, Yishi Su, Jie Zhang, Di Zhang, Enhanced mechanical properties of graphene (reduced graphene oxide)/aluminum composites with a bioinspired nanolaminated structure, Nano Lett. 15 (2015) 8077–8083.
[13] Biao Chen, Shufeng Li, Hisashi Imai, Lei Jia, Junko Umeda, Makoto Takahashi, Katsuyoshi Kondoh, An approach for homogeneous carbon nanotube dispersion in Al matrix composites, Mater. Des. 72 (2015) 1–8.
[14] S.R. Bakshi, D. Lahiri, Arvind Agarwal, Carbon nanotube reinforced metal matrix composites-a review, Int. Mater. Rev. 55 (2010) 41–64.
[15] Run Xu, Zhanqiu Tan, Dingbang Xiong, Genlian Fan, Qiang Guo, Jie Zhang, Yishi Su, Zhiqiang Li, Di Zhang, Balanced strength and ductility in CNT/Al composites achieved by flake powder metallurgy via shift-speed ball milling, Compos. Part A 96 (2017) 57–66.
[16] Hisao Uozumi, Kenta Kobayashi, Kota Nakanishi, Tadashi Matsunaga, Kenji Shinozaki, Hiroki Sakamoto, Takayuki Tsukada, Chitoshi Masuda, Makoto Yoshida, Fabrication process of carbon nanotube/light metal matrix composites by squeeze casting, Mater. Sci. Eng. A 495 (2008) 282–287.
[17] T. Laha, Y. Chen, D. Lahiri, Arvind Agarwal, Tensile properties of carbon nanotube reinforced aluminum nanocomposite fabricated by plasma spray forming, Composi. Part A 40 (2009) 589–594.
[18] Wenhua Ma, Yingchun Xie, Chaoyue Chen, Hirotaka Fukanuma, Jiang Wang, Zhongming Ren, Renzhong Huang, Microstructural and mechanical properties of high-performance Inconel 718 alloy by cold spraying, J. Alloys Compd. 792 (2019) 456–467.
[19] Wenya Li, Congcong Cao, Shuo Yin, Solid-state cold spraying of Ti and its alloys: a literature review, Prog. Mater. Sci. (2019) 100633.
[20] Xinliang Xie, Chaoyue Chen, Gang Ji, Run Xu, Zhanqiu Tan, Yingchun Xie, Zhiqiang Li, Hanlin Liao, A novel approach for fabricating a CNT/AlSi composite with the self-aligned nacre-like architecture by cold spraying, Nano Mater. Sci. (2019) 137–141.
[21] Xinliang Xie, Yu Ma, Chaoyue Chen, Gang Ji, Christophe Verdy, Hongjian Wu, Zhe Chen, Sheng Yuan, Bernard Normand, Shuo Yin, Cold spray additive manufacturing of metal matrix composites (MMCs) using a novel nano-TiB2-reinforced 7075Al powder, J. Alloys Compd. 819 (2020) 152962.
[22] Anatolii Papyrin, Cold spray technology, Adv. Mater. Process. 159 (2001) 49–51.
[23] Xinkun Suo, Xueping Guo, Wenya Li, Marie-Pierre Planche, Rodolphe Bolot, Hanlin Liao, Christian Coddet, Preparation and characterization of magnesium coating deposited by cold spraying, J. Mater. Process. Technol. 212 (2012) 100–105.
[24] Richard Jenkins, Barry Aldwell, Shuo Yin, Subhash Chandra, Gary Morgan, Rocco Lupoi, Solid state additive manufacture of highly-reflective Al coatings using cold spray, Opt. Laser Technol. 115 (2019) 251–256.
[25] Wen Sun, Adrian Wei-Yee Tan, Ayan Bhowmik, Fei Xue, Iulian Marinescu, Erjia Liu, Evaluation of cold sprayed graphene nanoplates–Inconel 718 composite coatings, Surf. Coat. Technol. 378 (2019), 125065.
[26] Srinivasa R. Bakshi, Virendra Singh, Kantesh Balani, D. Graham McCartney, Sudipta Seal, Arvind Agarwal, Carbon nanotube reinforced aluminum composite coating via cold spraying, Surf. Coat. Technol. 202 (2008) 5162–5169.
[27] Kicheol Kang, Gyuyeol Bae, Juyeon Won, Changhee Lee, Mechanical property enhancement of kinetic sprayed Al coatings reinforced by multi-walled carbon nanotubes, Acta Mater. 60 (2012) 5031–5039.
[28] Kicheol Kang, Jaeick Kim, Hyungkwon Park, Changhee Lee, Formation and heat treatment of kinetic sprayed nanocrystalline Al coatings reinforced with multi-walled carbon nanotubes: the relationship between microstructural features and physical properties, Surf. Coat. Technol. 289 (2016) 124–135.
[29] Yingchun Xie, Marie-Pierre Planche, Rija Raoelison, Philippe Hervé, Xinkun Suo, Pengjiang He, Hanlin Liao, Investigation on the influence of particle preheating temperature on bonding of cold-sprayed nickel coatings, Surf. Coat. Technol. 318 (2017) 99–105.
[30] Chaoyue Chen, Xinliang Xie, Yingchun Xie, Xincheng Yan, Chunjie Huang, Sihao Deng, Zhongming Ren, Hanlin Liao, Metallization of polyether ether ketone (PEEK) by copper coating via cold spray, Surf. Coat. Technol. 342 (2018) 209–219.
[31] American Society for Testing, Materials, ASTM West Conshohocken (PA), 2001.
[32] Srinivasa R. Bakshi, Virendra Singh, Sudipta Seal, Arvind Agarwal, Aluminum composite reinforced with multiwalled carbon nanotubes from plasma spraying of spray dried powders, Surf. Coat. Technol. 203 (2009) 1544–1554.
[33] Hamid Assadi, Frank Gärtner, Thorsten Stoltenhoff, Heinrich Kreye, Bonding mechanism in cold gas spraying, Acta Mater. 51 (2003) 4379–4394.
[34] Shuo Yin, Xiaofang Wang, Wenya Li, Hanlin Liao, Hongen Jie, Deformation behavior of the oxide film on the surface of cold sprayed powder particle, Appl. Surf. Sci. 259 (2012) 294–300.
[35] Wen-Ya Li, Hanlin Liao, Chang-Jiu Li, Hee-Seon Bang, C. Coddet, Numerical simulation of deformation behavior of Al particles impacting on Al substrate and effect of surface oxide films on interfacial bonding in cold spraying, Appl. Surf. Sci. 253 (2007) 5084–5091.
[36] W.Y. Li, C.J. Li, H.L. Liao, Significant influence of particle surface oxidation on deposition efficiency, interface microstructure and adhesive strength of cold-sprayed copper coatings, Appl. Surf. Sci. 256 (2010) 4953–4958.
[37] D.J. Woo, F.C. Heer, L.N. Brewer, J.P. Hooper, S. Osswald, Synthesis of nanodiamond-reinforced aluminum metal matrix composites using cold-spray deposition, Carbon 86 (2015) 15–25.
[38] Richard Jenkins, Shuo Yin, Barry Aldwell, Morten Meyer, Rocco Lupoi, New insights into the in-process densification mechanism of cold spray Al coatings: low deposition efficiency induced densification, J. Mater. Sci. Technol. 35 (2018) 427–431.
[39] Ningsong Fan, Jan Cizek, Chunjie Huang, Xinliang Xie, Zdenek Chlup, Richard Jenkins, Rocco Lupoi, Shuo Yin, A new strategy for strengthening additively manufactured cold spray deposits through in-process densification, Addit. Manuf. (2020) 101626.
[40] Biao Chen, Lei Jia, Shufeng Li, Hisashi Imai, Makoto Takahashi, Katsuyoshi Kondoh, In situ synthesized Al4C3 nanorods with excellent strengthening effect in aluminum matrix composites, Adv. Eng. Mater. 16 (2014) 972–975.
[41] Laipeng Yan, Zhanqiu Tan, Gang Ji, Zhiqiang Li, Genlian Fan, Dominique Schryvers, Aidang Shan, Di Zhang, A quantitative method to characterize the Al4C3-formed interfacial reaction: the case study of MWCNT/Al composites, Mater. Charact. 112 (2016) 213–218.
[42] Mildred S. Dresselhaus, G. Dresselhaus, R. Saito, A. Jorio, Raman spectroscopy of carbon nanotubes, Phys. Rep. 409 (2005) 47–99.
[43] Mildred S. Dresselhaus, Ado Jorio, Mario Hofmann, Gene Dresselhaus, Riichiro Saito, Perspectives on carbon nanotubes and graphene Raman spectroscopy, Nano Lett. 10 (2010) 751–758.
[44] R. Saito, M. Hofmann, G. Dresselhaus, A. Jorio, M.S. Dresselhaus, Raman spectroscopy of graphene and carbon nanotubes, Adv. Phys. 60 (2011) 413–550.
[45] R. George, K.T. Kashyap, R. Rahul, S. Yamdagni, Strengthening in carbon nanotube/aluminium (CNT/Al) composites, Scr. Mater. 53 (2005) 1159–1163.
[46] Hyunjoo Choi, Jaehyuck Shin, Byungho Min, Junsik Park, Donghyun Bae, Reinforcing effects of carbon nanotubes in structural aluminum matrix nanocomposites, J. Mater. Res. 24 (2009) 2610–2616.
[47] R. Huang, H. Fukanuma, Study of the influence of particle velocity on adhesive strength of cold spray deposits, J. Therm. Spray Technol. 21 (2012) 541–549.
[48] Dina Goldbaum, J. Michael Shockley, Richard R. Chromik, Ahmad Rezaeian, Stephen Yue, Jean-Gabriel Legoux, Eric Irissou, The effect of deposition conditions on adhesion strength of Ti and Ti6Al4V cold spray splats, J. Therm. Spray Technol. 21 (2012) 288–303.
[49] Shuo Yin, Xinkun Suo, Yingchun Xie, Wenya Li, Rocco Lupoi, Hanlin Liao, Effect of substrate temperature on interfacial bonding for cold spray of Ni onto Cu, J. Mater. Sci. 50 (2015) 7448–7457.
[50] T. Stoltenhoff, C. Borchers, F. Gärtner, H. Kreye, Microstructures and key properties of cold-sprayed and thermally sprayed copper coatings, Surf. Coat. Technol. 200 (2006) 4947–4960.
[51] Shuo Yin, Pengjiang He, Hanlin Liao, Xiaofang Wang, Deposition features of Ti coating using irregular powders in cold spray, J. Therm. Spray Technol. 23 (2014) 984–990.
[52] Niels Hansen, Hall–Petch relation and boundary strengthening, Scr. Mater. 51 (2004) 801–806.
[53] C. Borchers, F. Gärtner, T. Stoltenhoff, H. Kreye, Microstructural bonding features of cold sprayed face centered cubic metals, J. Appl. Phys. 96 (2004) 4288–4292.